Along-Strike Variations of the Partitioning of Convergence across the Haiyuan Fault System Detected by InSAR

Simon Daout, Romain Jolivet, Cécile Lasserre, Marie-Pierre Doin, Sylvain Barbot, Paul Tapponnier, Gilles Peltzer, Anne Socquet, Jianbao Sun

Geophysical Journal International

Geophys. J. Int. (2016) **205,** 536–547
GJI Geodynamics and tectonics

doi: 10.1093/gji/ggw028

Along-strike variations of the partitioning of convergence across the Haiyuan fault system detected by InSAR

S. Daout,[1] R. Jolivet,[2,*] C. Lasserre,[1] M.-P. Doin,[1] S. Barbot,[3] P. Tapponnier,[3] G. Peltzer,[4] A. Socquet[1] and J. Sun[5]

[1] *ISTerre, CNRS, Université Grenoble-Alpes, France. E-mail: simon.daout@ujf-grenoble.fr*
[2] *COMET, Bullard Laboratories, Department of Earth Sciences, University of Cambridge, CB3 0EZ, United Kingdom*
[3] *Earth Observatory of Singapore, Singapore*
[4] *Department of Earth Science, University of California, Los Angeles, CA, USA*
[5] *State Key Laboratory of Earthquake Dynamics, Institute of Geology, CEA, Beijing, China*

Accepted 2016 January 18. Received 2016 January 15; in original form 2015 July 31

SUMMARY

Oblique convergence across Tibet leads to slip partitioning with the coexistence of strike-slip, normal and thrust motion on major fault systems. A key point is to understand and model how faults interact and accumulate strain at depth. Here, we extract ground deformation across the Haiyuan Fault restraining bend, at the northeastern boundary of the Tibetan plateau, from Envisat radar data spanning the 2001–2011 period. We show that the complexity of the surface displacement field can be explained by the partitioning of a uniform deep-seated convergence. Mountains and sand dunes in the study area make the radar data processing challenging and require the latest developments in processing procedures for Synthetic Aperture Radar interferometry. The processing strategy is based on a small baseline approach. Before unwrapping, we correct for atmospheric phase delays from global atmospheric models and digital elevation model errors. A series of filtering steps is applied to improve the signal-to-noise ratio across high ranges of the Tibetan plateau and the phase unwrapping capability across the fault, required for reliable estimate of fault movement. We then jointly invert our InSAR time-series together with published GPS displacements to test a proposed long-term slip-partitioning model between the Haiyuan and Gulang left-lateral Faults and the Qilian Shan thrusts. We explore the geometry of the fault system at depth and associated slip rates using a Bayesian approach and test the consistency of present-day geodetic surface displacements with a long-term tectonic model. We determine a uniform convergence rate of 10 [8.6–11.5] mm yr^{-1} with an N89 [81–97]°E across the whole fault system, with a variable partitioning west and east of a major extensional fault-jog (the Tianzhu pull-apart basin). Our 2-D model of two profiles perpendicular to the fault system gives a quantitative understanding of how crustal deformation is accommodated by the various branches of this thrust/strike-slip fault system and demonstrates how the geometry of the Haiyuan fault system controls the partitioning of the deep secular motion.

Key words: Time-series analysis; Inverse theory; Radar interferometry; Kinematics of crustal and mantle deformation; Asia.

1 INTRODUCTION

Present-day tectonics in Asia results from the India-Eurasa collision, which initiated about 55 million years ago (e.g. Jaeger *et al.* 1989) and continues today at a velocity of about 4 cm yr^{-1} (e.g. Molnar & Tapponnier 1975; Tapponnier & Molnar 1977; Wang *et al.* 2001). Oblique convergence observed across the Tibetan plateau is accommodated by extrusion along major fault systems as well as crustal thickening resulting from successive accretionary wedges from the southwest to the northeastern boundary of the plateau (e.g. Métivier *et al.* 2007; Meyer *et al.* 1998; Tapponnier *et al.* 2001). Crustal deformation is partitioned between major strike-slip faults (e.g. Haiyuan, Altyn Tagh, Kunlun, Karakorum faults) and thrust fault systems (e.g. Himalaya, Qilian Shan, Lungmen Shan thrusts). These fault systems are responsible for devastating M ∼ 7.5-8 earthquakes, including strike-slip events [e.g. 1920 Haiyuan

*Now at: Departement de Géoscience, École Normale Supérieure, PSL Research University, F-75231 Paris, France.

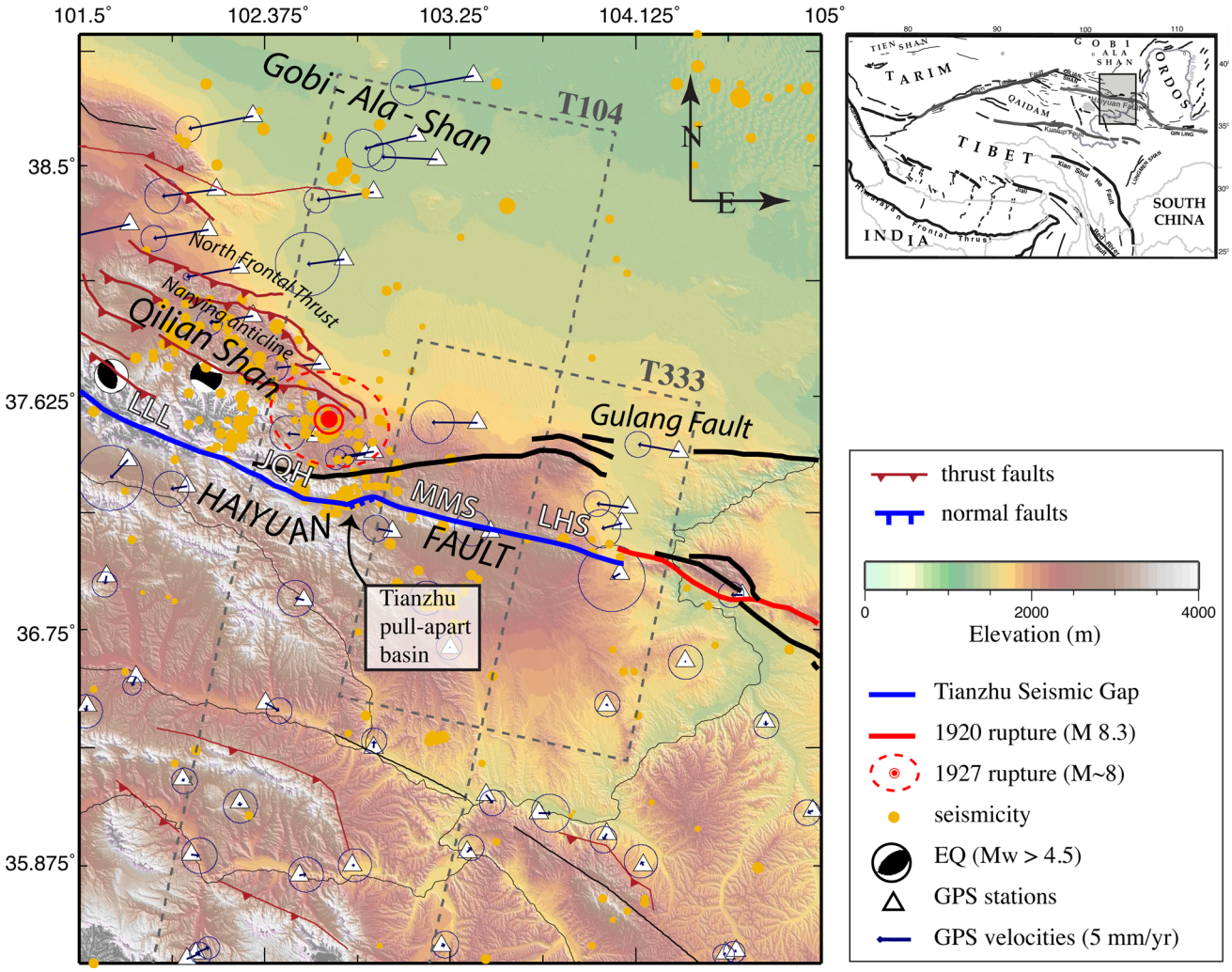

Figure 1. Seismotectonic setting of the Haiyuan fault system. The focal mechanisms of earthquakes of magnitude >5 from 2000 to 2014 are from USGS. Yellow dots show seismicity from 1988 to 2009 recorded by the Seismological Institute of Lanzhou. Blue arrows are GPS data from the Observation Network of China (ONOC; Liang *et al.* 2013) (in the South Haiyuan block reference frame). Dashed rectangles show the footprint of ENVISAT descending tracks 104 and 333. The Haiyuan–Gulang fault system is outlined in black, the Tianzhu seismic gap, unbroken since ∼ 1000 yr, in blue, and the 1920 and 1927 Haiyuan and Gulang rupture traces in red. The Tianzhu seismic gap is segmented in four segments from west to east: the Leng Long Ling (LLL), Jing Qiang He (JQH), Maomao Shan (MMS) and Lao Hu Shan (LHS) segments. The North Frontal Thrust (NFT) separates the Qilian Shan from the desert platform to the north. Inset at top right shows the location of the figure.

(Deng *et al.* 1986) and 2001 Kokoxili earthquakes (Lasserre *et al.* 2005)] and thrust events [e.g. 1927 Gulang (Gaudemer *et al.* 1995) and 2008 Wenchuan earthquakes (Shen *et al.* 2009)]. Modelling the kinematics and the partitioning of the deformation on active structures is thus essential to estimate their potential seismic hazard.

Here, we focus on the southeastern end of the Qilian Shan mountain range, where the Qilian thrusts connect to the Haiyuan left-lateral fault system, at the northeastern boundary of the Tibetan plateau (e.g. Gaudemer *et al.* 1995; Lasserre *et al.* 2002; Liu-Zeng *et al.* 2007; Cavalié *et al.* 2008; Jolivet *et al.* 2012). We use geodetic data (SAR interferometry—InSAR—and GPS) to quantify present-day displacement rates across three main structures: (1) the Qilian thrusts, ∼30 km north of the Haiyuan Fault, that ruptured during the $M \sim 8$, 1927 earthquake, (2) the left-lateral Gulang Fault, and (3) the central section of the left-lateral Haiyuan Fault, unbroken for more than 1000 yr, referred to as the Tianzhu seismic gap (Gaudemer *et al.* 1995; Fig. 1). This seismic gap, which extends for more than 250 km, is divided into four segments from west to east (Liu-Zeng *et al.* 2007): (1) the Leng Long Ling (LLL) segment west of the Gulang-Haiyuan triple junction, (2) the Jing Qiang He (JQH) segment, (3) the Maomao Shan (MMS) segment, and (4) the Lao Hu Shan (LHS) segment. The Haiyuan Fault is marked by a major left-lateral step over: the 10 km wide Tianzhu pull-apart basin, separating the JQH and MMS segments (Fig. 1). The basin marks a geometrical transition between the eastern Haiyuan fault system, where deformation is observed on the Haiyuan and Gulang strike-slip faults connected through a décollement, and the western Haiyuan fault system, where strain is partitioned between the Haiyuan Fault and the Qilian Shan thrust fault system forming a seismically active transpressional bend (Gaudemer *et al.* 1995; Lasserre *et al.* 2001; Fig. 2). Along the western fault system, Gaudemer *et al.* (1995) proposed that thrust faults and the Haiyuan Fault root on a 10°−20° south-dipping décollement, forming a typical 'flower structure' across this strike-slip restraining bend of the fault. South of the Haiyuan Fault, slip on a sub-horizontal, intra-crustal décollement is oblique to the orientation of the Haiyuan Fault (blue

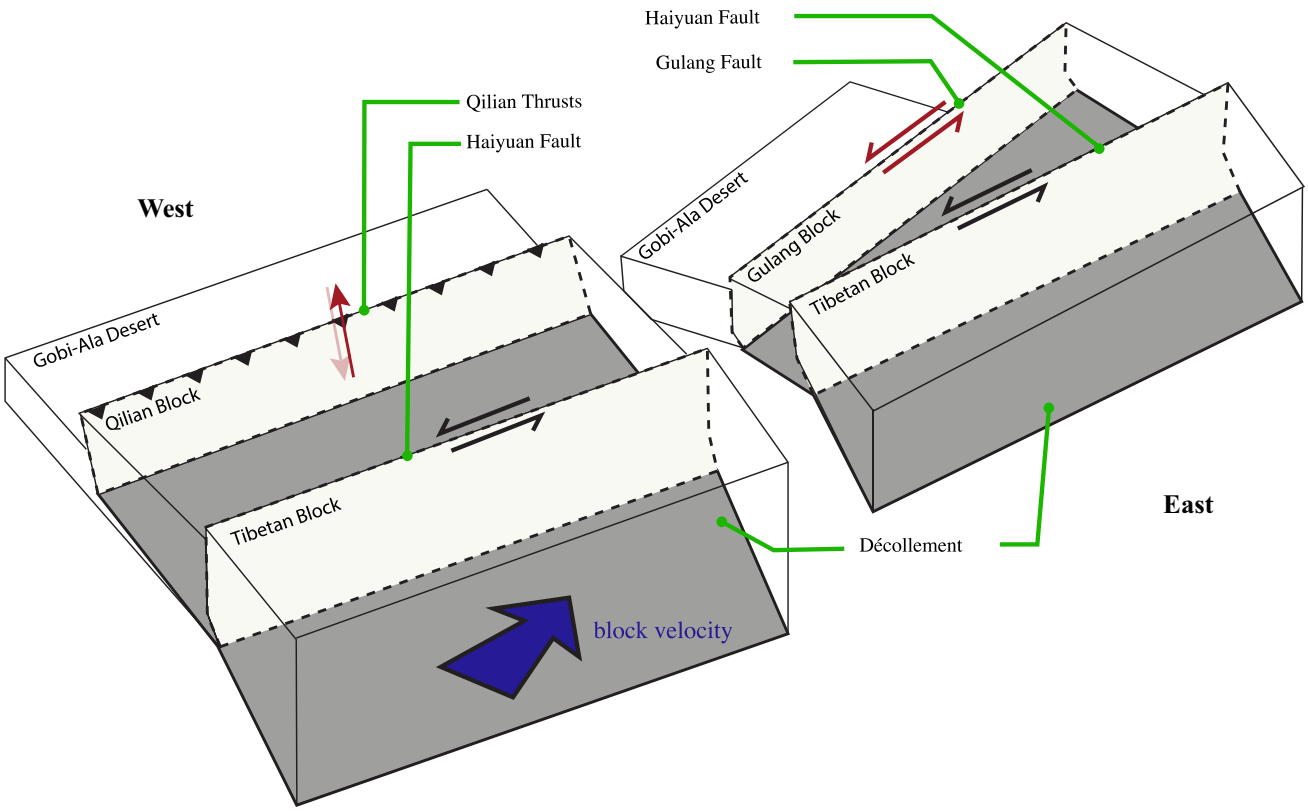

Figure 2. Schematic block model across the Haiyuan fault system illustrating the variation of slip partitioning west (left) and east (right) of the Tianzhu pull-apart basin. The oblique deep secular motion (large blue arrow) is accommodated by a deep crustal décollement below the brittle-ductile transition. The transpressional Qilian block is decoupled from Tibetan plateau by the vertical left-lateral Haiyuan fault and the south-dipping Qilian Shan thrusts. Identically, the Gulang block is bounded by the Haiyuan and Gulang left-lateral Faults that root in the décollement.

vector in Fig. 2) and accommodates both convergence (red vectors in Fig. 2) and transform components (black vector in Fig. 2) of the relative block motion. Recent broadband seismic survey from Ye *et al.* (2015) illuminates, at the root of the Haiyuan Fault, the underthrusting of the mantle of the North China lithosphere beneath the Qilian ranges and the presence of large scale intra-crustal décollements in the crust. These results support the Haiyuan tectonic model defined by Gaudemer *et al.* (1995) or the large scale model proposed by Tapponnier *et al.* (1990), Meyer *et al.* (1998) and Tapponnier *et al.* (2001), in which the Tibetan plateau has formed by successive crustal thickening and shortening bounded by major lithospheric faults.

We evaluate the compatibility of contemporary geodetic displacement rates with these models at different scales, which include partitioning of slip on strike-slip and thrust structures to explain the kinematics of oblique convergence across the Haiyuan fault system. We use GPS-derived velocities from Liang *et al.* (2013) and we derive maps of the average ground velocity using InSAR data from two tracks crossing the Haiyuan fault system, acquired along descending orbits by the Envisat satellite between 2003 and 2011 (Fig. 1). We first describe some strategic InSAR processing steps applied to increase the signal-to-noise ratio across the Haiyuan Fault. We then develop a 2-D model based on a Bayesian approach to invert two independent GPS and InSAR-derived LOS velocity profiles, on both sides of the Tianzhu basin, exploring the differences in the way slip is partitioned between the various active structures. We show that InSAR data helps to constrain the fault geometry and present-day kinematics, and we discuss the consistency of our interseismic deformation model with long-term tectonic models.

2 GPS VELOCITY FIELD

We use the GPS velocity field provided by Liang *et al.* (2013), that includes 750 continuous and campaign stations around the Tibetan Plateau spanning over 10 yr since 1999. We rotate the GPS solution with respect to a rigid block bounded by the Haiyuan fault, to the south of it. To do so, we select a subset of stations south of the Haiyuan fault to estimate an Eulerian rotation pole (Supporting Information Fig. S2a). All these stations are selected far from any faults to avoid trade-off between block rotation and interseismic deformation (Socquet *et al.* 2006). We invert for an Eulerian pole by minimizing the L1 norm of the ITRF08 velocities of this subset of stations. Our solution shows almost no residual velocities between observations and predictions indicating no internal deformation in this block south of the Haiyuan Fault (Supporting Information Fig. S2b). We then remove the predicted rotation by applying a Helmert transformation (Bevis & Brown 2014) in order to reference the GPS velocity field with respect to the South Haiyuan block (Fig. 1).

3 InSAR VELOCITY FIELD

In addition to GPS data, we use SAR data on two descending tracks of the Envisat satellite. InSAR ground velocity map on track 333 (Fig. 1) is from Jolivet *et al.* (2012). Moreover, we process all the 31 available SAR data acquired by the ENVISAT satellite on descending track 104, using the NSBAS chain based on the ROI_PAC software (Rosen *et al.* 2004; Doin *et al.* 2015). From the raw data, we first compute all Single Look Complex (SLC) images with a

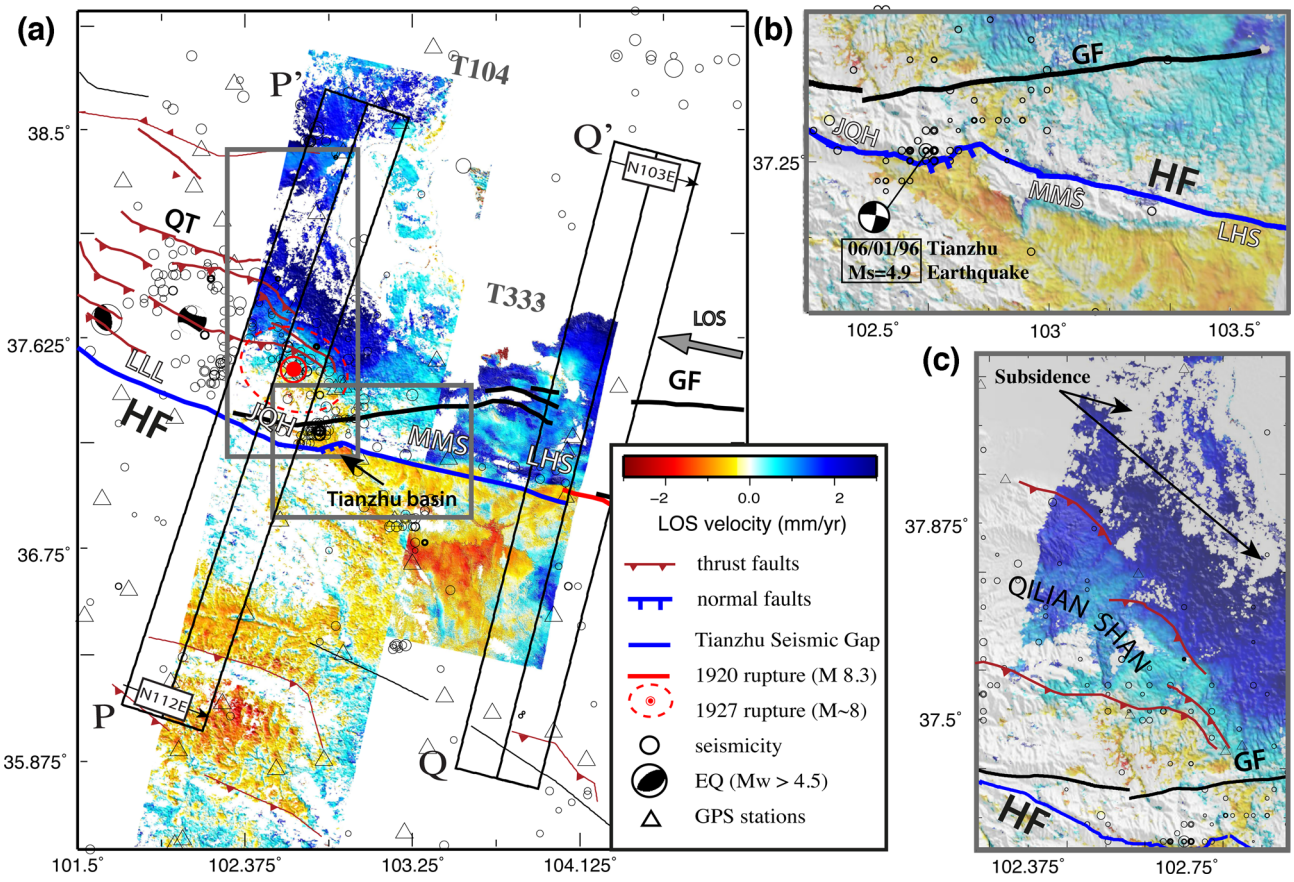

Figure 3. (a) Line of sight velocity maps for track 104 (left) and track 333 (right) showing a transition in the slip partitioning on both sides of the Tianzhu pull-apart basin. Positive motion is away from the satellite. Faults, GPS network and seismicity are as in Fig. 1. We define two profiles perpendicular to the Haiyuan fault (black rectangles), west (PP′) and east (QQ′) of the basin. The Jing Qiang He (JQH) segment, the Lao Hu Shan (LHS) segment, the Qilian shan Thrusts (QT) and the Gulang Fault (GF) represent the faults segments used in our model. (b) Zoom around the Tianzhu pull-apart basin showing a change in the fault locking depth between the MMS and the LHS segments. (c) Zoom around the Qilian Shan front bounding a zone of seismicity and uplift to the south and a zone of subsidence north of the thrusts. Panels (b) and (c) are superimposed to the SRTM Digital Elevation Model.

common Doppler bandwidth. We coregister the SLCs to a single master image chosen on the basis of maximum theoretical coherence (Hooper *et al.* 2007). We then compute differential interferograms, with 4 looks in range and 20 in azimuth (refer to Supporting Information Fig. S1 for interferogram network). The change in elevation between the desert of the Gobi Ala Shan platform (<1000 m), north of the Haiyuan fault (Fig. 1), and the mountain ranges (~4000 m), across and south of the fault, leads to significant atmospheric delays and possible topographic errors, affecting the coherence and our unwrapping capability of the InSAR data. To improve coherence over areas with rough topography and produce a continuous map of displacement, we use the newly developed tools in the NSBAS interferometric chain (Doin *et al.* 2015), including corrections of atmospheric delays and local Digital Elevation Model (DEM) errors before unwrapping (Jolivet *et al.* 2011; Ducret *et al.* 2014). These corrections are of particular importance as they reduce the fringe rate and phase noise across regions with high topographic gradients, hence preventing unwrapping errors. Tropospheric delays are predicted from the global atmospheric re-analysis ERA-Interim (ERA-I) computed by the European Center for Medium-Range Weather Forecast (ECMWF; Doin *et al.* 2009; Jolivet *et al.* 2011, 2014). We then multilook again 8 times in range and 40 times in azimuth, apply a low pass filter and unwrap the phase. The unwrapping path varies with the phase colinearity (Pinel-Puyssegur *et al.* 2012), avoiding the unwrapping of incoherent areas (Grandin *et al.* 2012; Doin *et al.* 2015). We derive the ground velocity along the line-of-sight (LOS) using a modified Small Baseline Subset time-series Analysis (SBAS), including a temporal constraint for pixels covered by disconnected subsets of interferograms (Cavalié *et al.* 2007; López-Quiroz *et al.* 2009). Finally, we remove residual unwrapping errors using an iterative procedure based on misclosure analysis of the interferometric network. At each iteration, misclosure maps are checked by visual inspection. Unwrapping errors are then corrected for each interferogram and times series analysis is iterated (López-Quiroz *et al.* 2009; Doin *et al.* 2011). A more detailed discussion of the processing as well as additional figures that allow for assessment of the quality of InSAR corrections are available in the Supporting Information (Supporting Information Fig. S3 for tropospheric corrections, Supporting Information Fig. S4 for local DEM errors corrections and Supporting Information Fig. S5 for velocity map).

The LOS velocity maps provide a continuous view of the surface displacement field over each track highlighting the contribution of active structures (Fig. 3). To first order, ground velocity suggests different patterns of strain accumulation on both sides of the 10 km wide Tianzhu basin (Fig. 3). In the following, we analyse two profiles of LOS velocity (50 km wide and 300 km long) perpendicular to the Haiyuan fault, east and west of the Tianzhu basin, where the Haiyuan fault strikes $N103°E$ and $N112°E$, respectively (Figs 3–5), and explore the apparent change of strain

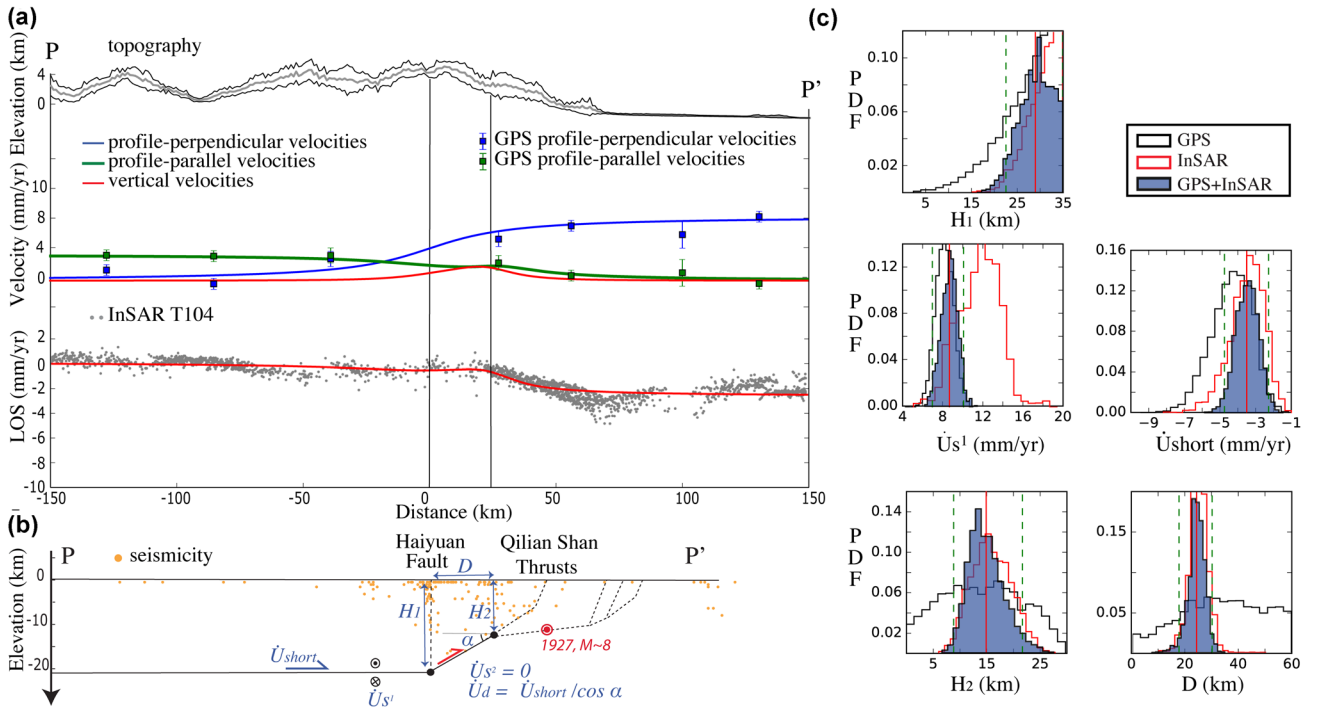

Figure 4. Inversion model and results for profile PP′ west of the Tianzhu basin. (a) Top: topography (grey line for the average topography and black dash-lines for the maximum and minimum topography). Middle: profile-parallel (green square markers) and profile-perpendicular (blue square markers) GPS velocities with their associated 1σ uncertainties. Average model obtained (corresponding blue, green and red lines) along profiles. Bottom: LOS velocities (grey points). (b) Fault geometry and fault velocities parameters explored in the inversion; solid (resp. dashed) lines represent slipping (resp. locked) sections of the faults; free parameters are in blue; arrows indicate relative direction of slip on faults. (c) Posterior marginal PDF using the GPS data only or the InSAR data only (black and red unfilled histograms, respectively) or the GPS+InSAR data (blue histograms), illustrating the slip partitioning across the fault system and the benefits of including the InSAR data. See the text for further details on model setting.

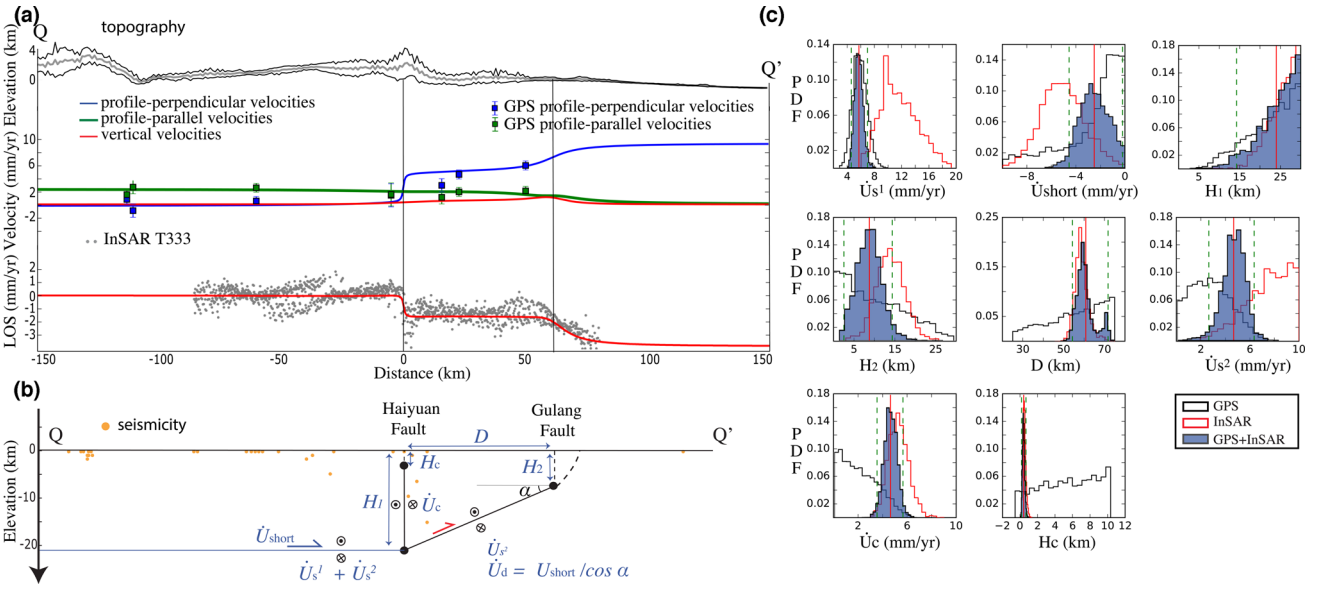

Figure 5. Same as Fig. 4, but for the eastern profile QQ′.

accumulation along strike. Along the eastern fault section (LHS and MMS segments; Figs 3b and 5a), we observe localized high strain along the Haiyuan fault, due to creep along the seismogenic portion of the fault (Cavalié *et al.* 2008; Jolivet *et al.* 2012, 2013, 2015a). The strain pattern observed 60–70 km north of the Haiyuan fault is consistent with left-lateral motion along the Gulang Fault (Jolivet *et al.* 2012) (Fig. 3b). Along the western section (LLL and JQH segments), the velocity map and profile reflect the combined effect of vertical motion associated with the Qilian Shan thrusts and of strike-slip motion on the Haiyuan fault (Figs 3c and 4a). With respect to the southern side of the Haiyuan fault, the northern side is moving ∼4 mm yr^{-1} in the LOS direction away from the satellite (Figs 3c and 4a). A zone of local subsidence is also observed ∼70 km north of the Haiyuan Fault in a region of sand dunes, at the foot of the Qilian thrusts. It might be of non-tectonic origin, related to water pumping.

4 2-D MODELS

To understand the kinematics and the partitioning of the deep-secular motion on both sides of the Tianzhu pull-apart basin, we test the model proposed by Gaudemer *et al.* (1995) from geological observations (Fig. 2). We adjust the fault geometry and estimate corresponding slip rates using a Bayesian approach on the InSAR and GPS data projected on two independent profiles. The two profiles are on both sides of the Tianzhu pull-apart basin and perpendicular to the Haiyuan Fault. We test whether the apparent east–west variability of the strain pattern is consistent with the model of partitioning of the convergence on the structures observed at the surface (Fig. 3).

4.1 Model geometry

For both profiles, the model consists of 2-D dislocations, infinite in the along-strike dimension, embedded in a homogeneous elastic half-space. The model includes both semi-infinite and finite dislocations accounting for deformation at shallow depth. We model the flat décollement by a horizontal semi-infinite dislocation, limited to the north by the Haiyuan fault, with oblique motion (both strike-slip and dip-slip). We extend the décollement with a ramp, connecting the northern tip of the décollement to the down-dip end of locked faults in the seismogenic part of the crust (Figs 4b–5b). A detailed description of each dislocation used to build the models in Figs 4(b) and 5(b) is available in the Supporting Information (Fig. S6). For the eastern profile, the ramp points towards the Gulang Fault, oblique to the profile. We allow for creep on the shallow portion of the Haiyuan Fault on a vertical finite segment up to a shallow locking depth. For the western profile, the ramp points towards the foot of the Qilian Shan thrusts.

4.2 Free parameters

We assume a horizontal décollement, so that the dip-slip component on this flat structure, $\dot{U}_{\text{short}}$, is an effective estimate of the shortening rate perpendicular to the fault system (Figs 4b–5b). For both profiles, we estimate the depth, H_1, of the semi-infinite dislocation representing the décollement, as well as the slip rate parallel, $\dot{U}_{s1}$, and perpendicular, $\dot{U}_{\text{short}}$, to the Haiyuan fault system. Note that surface displacements due to the strike-slip component, $\dot{U}_{s1}$, are not influenced by the dip-angle of the structure. We test values of depth, H_1, between 0 and 30 km, left-lateral velocity, $\dot{U}_{s1}$, between 0 and 20 mm yr^{-1}, and of shortening rate, $\dot{U}_{\text{short}}$, between 0 and 10 mm yr^{-1}. For the shallow ramps, we estimate the horizontal distance between the tip of the décollement and the bottom of the locked section of the frontal fault, D (also called *width* of the system), the locking depth of the frontal fault, H_2, and the along-strike component of slip, $\dot{U}_{s2}$. The dip angle of the ramps are deduced from the parameters D, H_1 and H_2. The along-dip component of slip along the frontal structure is defined as the projection of the shortening, $\dot{U}_{\text{short}}$, along this dipping plane (McCaffrey 2002).

For the eastern profile (Fig. 5b), we test values of strike-slip motion on the Gulang Fault, $\dot{U}_{s2}$, between 0 and 10 mm yr^{-1}, of locking depth, H_2, between 0 and 30 km and of horizontal distance to the Haiyuan fault, D, between 25 and 75 km. On the vertical dislocation modelling creep on the Haiyuan fault, we test values of locking depth, H_c, between −0.5 and 10.5 km, and strike-slip component, $\dot{U}_c$, between 0 and 10 mm yr^{-1}. Note that we allow for non-physical negative values for the locking depth in order to better sample the 0 km value (full creeping of the seismogenic zone). Slip on the shallow dislocation, $\dot{U}_c$, is set lower or equal to $\dot{U}_{s1}$, allowing for a slip deficit on the creeping segment. Strike-slip on the Gulang fault is on a semi-infinite dislocation and the total strike-slip on the décollement is thus equal to the sum of $\dot{U}_{s1}$ and $\dot{U}_{s2}$ (Figs 5b and S6B).

For the western profile, we test values of locking depth of the Qilian Shan thrusts, H_2, between 0 and 30 km, of horizontal distance to the Haiyuan fault, D, between 0 and 60 km. Preliminary tests show that no creep is required on the western segment, so that we assume that the Haiyuan Fault is fully locked on this section. We consider no strike-slip motion on the Qilian Shan thrusts, consistent with geomorphological long-term observations (Gaudemer *et al.* 1995) (Fig. 4a and Supporting Information Fig. S6A).

4.3 Inversion method

We use a Bayesian approach to explore the range of models allowed by geodetic data, to provide realistic estimates of uncertainties and to avoid some of the issues related to the regularization of the inverse problem such as the choice of damping factor or normality assumptions (Minson *et al.* 2013). Bayes' rule writes the posterior probability density function (PDF) of a model, $p(\mathbf{m}|\mathbf{d})$ (i.e. what we know from the prior and the data), as proportional to the prior PDF, $p(\mathbf{m})$ (i.e. the knowledge before input from data), and the likelihood (i.e. a measure of the misfit), such as

$$p(\mathbf{m}|\mathbf{d}) \propto p(\mathbf{m})\exp\left[-\frac{1}{2}(\mathbf{d}-\mathbf{g}(\mathbf{m}))^T\mathbf{C}_d^{-1}(\mathbf{d}-\mathbf{g}(\mathbf{m}))\right], \quad (1)$$

where $\mathbf{d}$ is the vector of data, $\mathbf{m}$ is the vector of model parameters, $\mathbf{C}_\text{d}$ is the covariances matrix in the data space and $\mathbf{g(m)}$ is the surface displacements predicted using a model $\mathbf{m}$.

For both profiles, the model, $\mathbf{m}$, includes the parameters previously described for geometry and slip rates, as well as InSAR and GPS reference frames. An azimuthal ramp is included for the InSAR data to explore trade-off between residual long-wavelength orbital errors and slip rates. The data vector, $\mathbf{d}$, is made of the LOS displacement rates and GPS velocities projected into profile-perpendicular and profile-parallel components along each profile. The data covariance (i.e. describing uncertainties on observations), $\mathbf{C}_\text{d}$, includes the variance of the GPS measurements on its diagonal. For InSAR data, the covariance includes data variance as diagonal terms and data spatial correlation in the off-diagonal components. From data-model residuals of a preliminary inversion, we compute empirical covariance as a function of the distance between InSAR points on the residual velocity map (Lohman & Simons 2005; Sudhaus & Sigurjón 2009). We then estimate the best-fit exponential function to build the full data covariance (Chiles & Delfiner 2009; Jolivet *et al.* 2015b). Phase residual distributions, empirical covariances, best-fit functions and covariance matrix for InSAR data are shown in Supporting Information Fig. S7.

For each profile independently, we draw random samples from uniform distributions between the minimum and the maximum values defined for all parameters and evaluate the posterior PDF using the Metropolis algorithm implemented in the PyMC library (Metropolis *et al.* 1953; Patil *et al.* 2010). Our Markov chain has 20 000 iterations, rejecting the first 10 000 samples to minimize the effect of the initial model.

4.4 Inversion results

The complete comparison between the prior and posterior model distributions, as well as the first moments of the marginal posterior

distributions, are summarized in Table S1 of the Supporting Information. All the uncertainties are documented with their 95 per cent confidence interval.

For the western profile (Fig. 4), the mean posterior model suggests a depth of the décollement, H_1, of 25 [19–30] km, and sets the tip of the shallow ramp, H_2, at 15 [9–22] km. Our estimates also indicate a well-constrained width, D, of 24 [17.5–30] km, corresponding to a dip angle of the ramp of 21 [8–34] ° below the Qilian Shan. The left-lateral slip-rate, $\dot{U}_{s1}$, on the western section of the Haiyuan Fault (JQH segment) is 8.6 [6.9–10] mm yr^{-1} and the mean shortening rate across the whole system, $\dot{U}_{\text{short}}$, is 3.5 [2.3–4.8] mm yr^{-1}. All the five PDFs (Fig. 4c) resemble normal distributions centred on the mean model, with higher skewnesses for the PDFs of D and H_2 (Supporting Information Table S1).

For the eastern profile (Fig. 5), the mean model includes 5.6 [4.5–6.9] mm yr^{-1} of strike-slip motion along the Haiyuan Fault. The creep rate, $\dot{U}_c$, is of 4.6 [3.5–5.6] mm yr^{-1} between 0.5 [0.2–0.7] km (H_c) and 24 [14–30] km (H_1) depth. The depth of the Haiyuan Fault, H_1, is not well constrained, as illustrated in Fig. 5(c) and described by the first moments of the marginal distribution (Supporting Information Table S1). The corresponding shortening rate across the fault system, $\dot{U}_{\text{short}}$, is of 2.6 [0.2–4.6] mm yr^{-1}. Left-lateral velocity on the Gulang segment is of 4.6 [2.6–6.3] mm yr^{-1} with a locking depth of 9 [2.5–14.5] km. The width, D, is constrained at 61 [54–72] km, corresponding to a dip angle of 13.5 [5–21] °. PDFs of $\dot{U}_{s1}$, $\dot{U}_{\text{short}}$, H_c, H_2, $\dot{U}_{s2}$, $\dot{U}_c$, resemble normal distributions centred on the mean model (Fig. 5c, Supporting Information Table S1).

5 DISCUSSION

5.1 InSAR and Bayesian methods

In areas of high relief, significant atmospheric delays and DEM errors lead to spatial aliasing of the wrapped and filtered interferometric phase, resulting in unwrapping errors (Grandin *et al.* 2012). By flattening the interferometric phase with local DEM (Ducret *et al.* 2014) and tropospheric corrections (Cavalié *et al.* 2007; Doin *et al.* 2009; Jolivet *et al.* 2011), we significantly reduce the unwrapping errors and increase the total area of unwrapped phase over the Qilian ranges. This allows us to produce a continuous map across a region with more than 3000 m of elevation change and to study at large scale the kinematics of the fault system integrating all the structures. Unlike GPS measurements, InSAR has a strong sensitivity to vertical displacements and its high spatial resolution finely constrains strain localization and first order patterns of fault geometry. Moreover, the Bayesian method derives the range of possible values exploring the influence of fault geometry on surface displacements. To illustrate the contribution of InSAR data, we compare posterior model PDFs derived using GPS data only with those derived with InSAR data only, and those derived using both GPS and InSAR data (Figs 4c and 5c). On the eastern profile, due to the lack of GPS stations in the far-field, the Gulang fault parameters are only controlled by InSAR. Without InSAR data, D and H_c, the width of the system and the depth of creep, are not constrained, with uniform posterior PDFs close to the prior uniform model. InSAR constrains the localization of the deformation on a kilometric-wide zone and reveals no deformation between faults. For the other parameters, posterior PDFs obtained without InSAR data resemble normal distributions but are much wider than with the information enclosed in the InSAR data. Although limited by the spatial correlation of the noise, the LOS velocity maps help to constrain the gradient of deformation and thus the locking depths of fault segments. For example, the 2σ uncertainties of H_2 are equal to ∼14 km with GPS data only for the western and the eastern profiles, whereas while adding the InSAR data, uncertainties shrink to ∼6 km. However, using InSAR data only results in wider and biased PDFs for slip rates with respect to those obtained using GPS data only, because of the trade-off between long-wavelength residual signal and the deformation [see posterior correlation coefficient matrix of the free parameters for the western and eastern profiles (Supporting Information Tables S2 and S3) and joint marginal PDFs (Supporting Information Fig. S9) for illustrations of these trade-offs]. GPS data thus constrain the horizontal slip rates and the combination of InSAR and GPS together fixes the fault-system geometry.

5.2 Lateral variations of the slip partitioning

Our mean model indicates that horizontal shortening rates and left-lateral slip rates are differently distributed west and east of the Tianzhu basin. Along the western section, oblique convergence is purely partitioned with 3.5 [2.3–4.8] mm yr^{-1} of shortening across the northeastern Qilian Shan thrust system and 8.6 [6.9–10] mm yr^{-1} of left-lateral strike-slip motion on the Haiyuan Fault (Fig. 6a). In contrast, along the eastern section, our parameter exploration indicates that the left-lateral Gulang Fault accounts for 4.6 [2.6–6.3] mm yr^{-1} of strike-slip rate and 2.6 [0.2–4.6] mm yr^{-1} of shortening rate in directions perpendicular and parallel to the profile, respectively, whereas the Haiyuan Fault slips at a left-lateral rate of 5.6 [4.5–6.9] mm yr^{-1} at depth. This 2-D model implies a long-term slip vector along the Gulang fault system of 5.4 [3.7–7.0] mm yr^{-1} with an azimuth of 28 [1–51] ° with respect to the $N103E$°-striking Haiyuan Fault. This result is in agreement with the geometry of the Gulang Fault at the surface, which forms an angle of ∼20°−30 ° with the MMS and LHS segments of the Haiyuan Fault (Figs 3a and b, and Supporting Information Fig. S8) and absorbs the shortening component by its obliquity (see velocity vectors sum in Fig. 6b). In agreement with studies by Cavalié *et al.* (2008) and Jolivet *et al.* (2012, 2013, 2015a), our model shows that slip rate on the vertical creeping segment, $\dot{U}_c$, is on the same order as the Haiyaun Fault deep-seated rate, $\dot{U}_{s1}$. We evaluate the probability that no strain is presently accumulating on the Haiyuan Fault along the eastern profile (i.e. $\dot{U}_c$ is equal to $\dot{U}_{s1}$ and H_c is null). We found that 88 per cent of the models have a creep rate $\dot{U}_c$ equal to $\dot{U}_{s1}$ within 2 mm yr^{-1} and have a locking depth, H_c, shallower than 1 km, confirming a low probability of slip deficit buildup along the LHS portion of the Haiyuan Fault (Cavalié *et al.* 2008; Jolivet *et al.* 2012).

We then evaluate the probability for the far-field tectonic motion across the whole Haiyuan fault system (blue vector in Fig. 2) to be consistent on both sides of the Tianzhu pull-apart, comparing the azimuth and the norm of the convergence vectors for the eastern and the western profiles. To the west, the far-field tectonic convergence vector on the décollement is the sum of strike-slip motion along the Haiyuan Fault, $\dot{U}_{s1}$, and shortening across the fault system, $\dot{U}_{\text{short}}$ (Fig. 6a). To the east, the total convergence on the décollement is the sum of the combined strike-slip motion along the Haiyuan, $\dot{U}_{s1}$, and Gulang Fault, $\dot{U}_{s2}$, and the shortening component across the fault system, $\dot{U}_{\text{short}}$ (Fig. 6b). We find that 64 per cent of the models explaining the geodetic data show similar convergence rates within 2 mm yr^{-1} and similar azimuth within 20°. On average, to the west we estimate a convergence rate of 9.3 [7.8–10.8] mm yr^{-1} with an N89.5 [82–98] °E azimuth (Fig. 7) across the 24 [17.5–30] km wide

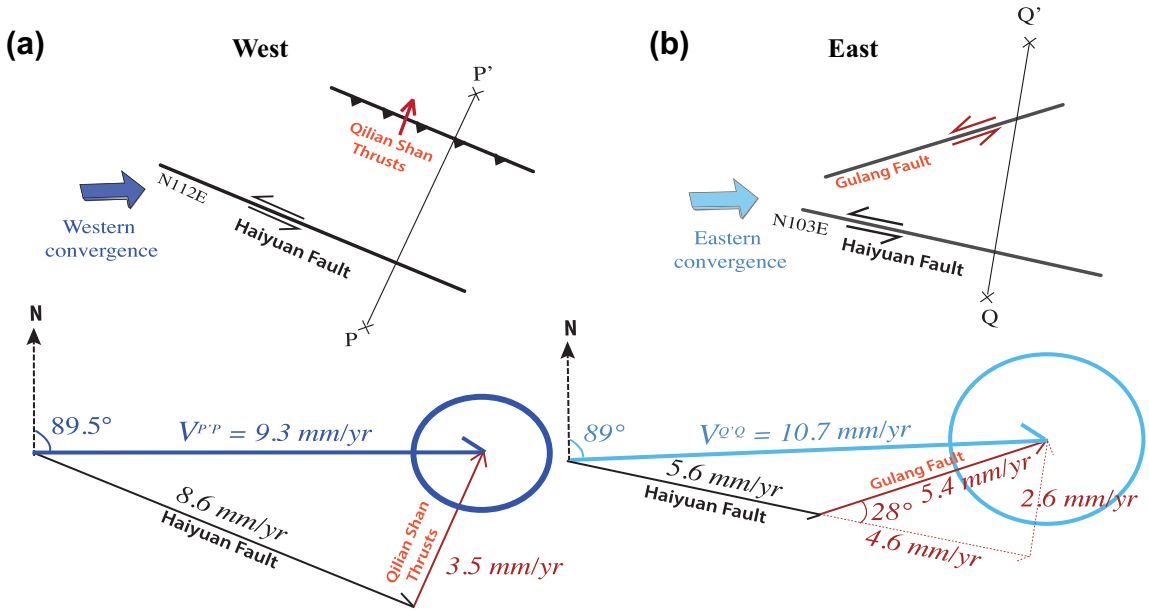

Figure 6. Kinematic sketch summarizing the longitudinal or lateral change in slip partitioning between the various branches of the fault system west (a) and east (b) of the Tianzhu pull-apart basin (after Gaudemer *et al.* 1995). Profiles PP′ and QQ′ are shown in map view in Fig. 3.

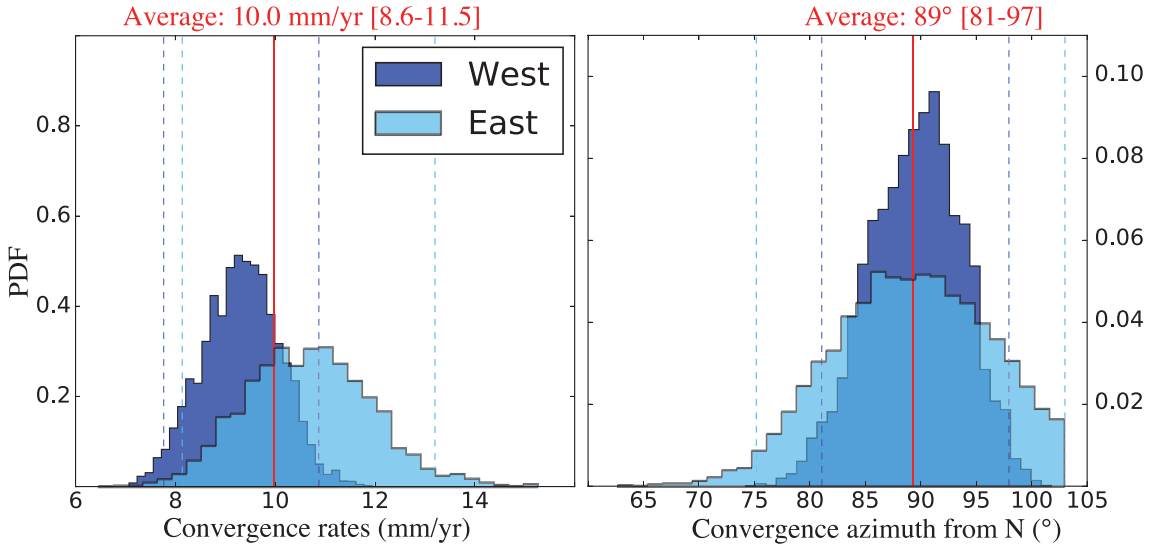

Figure 7. Posterior PDFs for the norm and the azimuth of the convergence vectors across the Haiyuan fault system for both profiles (blue vectors $V_{P'-P}$ and $V_{Q'-Q}$ on Fig. 6). Data constraints include both GPS and InSAR velocities.

fault-system partitioned between the $N112E^{\circ}$-striking left-lateral Haiyuan fault and the Qilian Shan thrusts that connect at a depth of 25 [19–30] km. To the east, we estimate a convergence rate of 10.7 [8.2–13.1] mm yr^{-1} with an N89 [77–103] °E azimuth (Fig. 7) across the 61 [54–72] km wide fault-system distributed in between the $N103E^{\circ}$-striking Haiyuan Fault and the Gulang Fault that merge at a depth of 24 [14–30] km. The present-day geodetic displacements may thus be explained with a long-term 'flower structure' model, with a uniform convergence rate of 10 [8.6–11.5] mm yr^{-1} with an N89 [81–97] °E across the whole fault system (Figs 6 and 7). Such consistency of the far-field tectonic motion implies that the connected thrusting and strike-slip faulting are thus complementary facets of the same deep-seated deformation process, participating into the growing and rising of the Tibetan plateau (Tapponnier *et al.* 2001).

In previously proposed block models with only vertical faults, results mostly depend on the prior choice of the number and shape of rigid blocks (Meade 2007; Thatcher 2007; Loveless & Meade 2011). These models can describe the first order geodetic deformation and account for 3-D spatial interaction between faults. However, they do not allow for local complexity of the structures, such as partitioning, or do not explore the lateral variations of locking depths, which leads to a uniform strike-slip rate along the various vertical segments of the Haiyuan Fault of ∼9 mm yr^{-1} [Meade (2007), without off-fault distributed deformation] or ∼6 mm yr^{-1} [Thatcher (2007), Loveless & Meade (2011), with internal micro-plate strain modelled by off-fault distributed deformation]. In comparison, our model explores the geometry of the fault-system at depth and the partitioning of the uniform deep-seated motion in between the various segments intervening in the upper crust. Our model allows us to

investigate both along-strike and fault-perpendicular variations of slip along the fault system and the corresponding trade-offs between fault rates and geometry. We show a decrease of the locking depth from 25 [19–30] km along western section (thus fully locked) to 0.5 [0.2−0.7] km along the eastern creeping section of the Haiyuan Fault, with different slip partitioning on both sides of the basin (Fig. 6a). Our model does not require any internal deformation to explain the current displacement rates and shows that most of the complexity of the surface velocity field across the Haiyuan fault system may be accounted for by partitioning, laterally and at depth.

5.3 Comparison with geological time scales

The geometry of our most likely model, assumed to be representative of the geometry over several seismic cycles, is consistent with the variation of the long-term topography observed on both sides of the Tianzhu basin. To the west, we infer a 21 [8–34] ° dip angle of the ramp, while to the east, our model suggests a dip angle of 13.5 [5–21] °. Topography is more pronounced to the west (max. of 4200 m in the Qilian Shan) than to the east (max. of 3000 m in the LHS). Shortening may be accommodated on a steeper ramp to the west than to the east, which is consistent with the idea that the change of geometry of the Haiyuan Fault from west to east controls the way convergence motion is partitioned, thus the amount of growing and extrusion of the Tibetan plateau (Meyer *et al.* 1998; Tapponnier *et al.* 2001).

The proposed ramp-décollement geometry is conceptual and represents a way of describing both elastic and permanent parts of surface displacement field at the present time. Over geological time scale, this geometry is unstable and non-conservative. The faults will propagate towards the north, deform and adapt for new configurations. Near the slope break at depth, the horizontal slip incompatibility may be accommodated by distributed deformation and by a kink-fault forming a fault-bend fold structure (Suppe 1983; Thompson *et al.* 2002). In another model, this residual velocity between the ramp and the décollement may also create a back-thrust or a normal fault decoupling the Qilian Shan block from the Tibetan block (Fig. 2) and forming a typical transpressive 'flower structure' tectonic model (Gaudemer *et al.* 1995).

InSAR and GPS indicate as much as 3.5 [2.3–4.8] mm yr^{-1} of deep-seated shortening motion accumulated during the interseismic period for the western section of the Haiyuan Fault. We find that 80 per cent of the models are in agreement with the 2.8 ± 1.3 mm yr^{-1} long-term slip rates measured by Champagnac *et al.* (2010) on the North Frontal Thrust (NFT) of the Qilian Shan (Fig. 1). More recently, Hu *et al.* (2015) measured, north of the Nanying anticline and south of the NFT (Fig. 1), a shortening rate of 0.9 ± 0.3 mm yr^{-1}, but we find no model in agreement with this range of values. On the other hand, we find that 99 per cent of the models lie within the shortening rate of 4.0 ± 2 mm yr^{-1} deduced by Gaudemer *et al.* (1995), from a kinematic sketch based on strike-slip rates of the Haiyuan and Gulang faults and the surface geometry of the fault system. This suggests that the shortening rate on the décollement might be accommodated by various thrust structures (Champagnac *et al.* 2010) or by folding (Hu *et al.* 2015) at different periods of the seismic cycle.

Based on levelling measurements of offset-terrace risers, Gaudemer *et al.* (1995) estimate a Holocene slip rate for the N112°E eastern JQH segment of the Haiyuan Fault of 11 ± 4 mm yr^{-1}. In comparison, our mean model shows a lower left-lateral rate of 8.6 [6.9–10] mm yr^{-1} along the western profile. However, we find than 96 per cent of the models explaining our geodetic data exhibit a strike-slip motion along the JQH segment that lies within the range of geological rates, between 7 and 15 mm yr^{-1}. Some discrepancies between short-term and long-term rates may come from the complex link between present-day measurements of strain accumulation at the surface, the long-term accumulation and release of strain along fault and surrounding medium, the temporal variations of interseismic slip rates throughout the seismic cycle of the fault (e.g. Hetland & Simons 2010; DeVries & Meade 2013; Meade *et al.* 2013), as well as the effect of the steep topography on the surface velocity field (Thompson *et al.* 2015).

5.4 Influence of the M∼8, 1920 Haiyuan and 1927 Gulang earthquakes

Transient processes triggered by previous earthquakes may also influence observed interseismic slip rates of the fault. Creep can potentially be initiated by coseismic stress changes as post-seimic afterslip from several years to decades after a large event (Hetland & Simons 2010; Çakir *et al.* 2012). Creep on the Haiyuan Fault is located at the western tip of the 1920 Haiyuan earthquake (Jolivet *et al.* 2012). Also we cannot exclude a possible residual post-seismic deformation in the area that ruptured during the 1927 M ∼ 8 Gulang earthquake, which caused major stress changes and is still seismically active (Fig. 1; Lasserre 2000; Lasserre *et al.* 2001). Integrating post-seismic deformation from previous large earthquakes in a comprehensive 3-D viscoelastic deformation model (Trubienko *et al.* 2013), may be important to further characterize the average interseismic strain accumulation in this region and take into account the interactions between faults, but is beyond the scope of the present work.

6 CONCLUSIONS

We produce a time-series analysis of InSAR data across a challenging mountainous area in northern Tibet. The processing procedure is based on a small baseline approach. To improve the signal-to-noise ratio and the phase unwrapping capability across the fault, we correct for tropospheric delays (using the ERA Interim Global Atmospheric Models) and local Digital Elevation Model errors before unwrapping and apply a series of filtering steps. We produce a velocity map of the present-day interseismic strain accumulation across the central Haiyuan Fault consistent with GPS data. The velocity map provides a continuous map of deformation over a large zone with a strong sensitivity to vertical motion, useful to assess the geometry of faults. We explain the present-day surface displacements with a slip partitioning model derived from a long-term structural and tectonic model. In the model, strike-slip and thrust faults branch off at depth on a deep décollement, which moves aseismically during the interseismic period. Using a fully Bayesian approach, we investigate the trade-off between fault geometry parameters and slip rates. InSAR data help to constrain the gradient and the localisation of the deformation. We constrain the variations of geometry and locking depths and highlight the benefits of adding InSAR data in the inversion, which decreases the uncertainties on the model parameters. We show the compatibility of the present-day displacement field with a long-term tectonic model and quantify a uniform convergence rate of 10 [8.6–11.5] mm yr^{-1} with an N89 [81–97] °E, across the whole fault system, partitioned differently west and east of the Tianzhu basin. To the west, oblique convergence is purely partitioned between the Haiyuan Fault, which accommodates left-lateral slip at

a rate of 8.6 [6.9–10] mm yr^{-1}, and the Qilian Shan thrusts, which absorb 3.5 [2.3–4.8] mm yr^{-1} of shortening. To the east (i.e. where the azimuth of the Haiyuan Fault changes slightly), the oblique convergence is partitioned between 5.6 [4.5–6.9] mm yr^{-1} of left-lateral motion along the Haiyuan Fault, 4.6 [2.6–6.3] mm yr^{-1} of left-lateral velocity along the Gulang Fault, and 2.6 [0.2–4.6] mm yr^{-1} of shortening along the oblique fault-system. These results illustrate the importance of the geometry of the Haiyuan fault system, controlling eastward motion and the growth of the crustal wedge at this boundary of the Tibetan plateau.

ACKNOWLEDGEMENTS

We thank Editor, Prof Duncan Agnew, and two anonymous reviewers for their thorough and thoughtful reviews of this manuscript. The SAR data set was provided by the European Space Agency (ESA) in the framework of the Dragon 3 program (projects ID 10686). The NSBAS development was funded through the CNES TOSCA program (SAR ready and TeraSAR projects). SD's work is supported through the Dragon 3 Young Scientist fellowship, Grenoble Innovation Recherche (AGIR) fellowship, two Labex OSUG@2020 University of Grenoble projects and the CNRS Mastodons computing facilities. Part of work was done at the Earth Observatory of Singapore, funded from the National Research Foundation and the Labex OSUG@2020 from University of Grenoble. RJ is supported by the Marie Currie FP7 Initial Training Network iTECC (investigating Tectonic Erosion Climate Coupling).

REFERENCES

Bevis, M. & Brown, A., 2014. Trajectory models and reference frames for crustal motion geodesy, *J. Geod.,* **88**(3), 283–311.

Çakir, Z., Ergintav, S., Özener, H., Dogan, U., Akoglu, A.M., Meghraoui, M. & Reilinger, R., 2012. Onset of aseismic creep on major strike-slip faults, *Geology,* **40**(12), 1115–1118.

Cavalié, O., Doin, M.-P., Lasserre, C. & Briole, P., 2007. Ground motion measurement in the Lake Mead area, Nevada, by differential synthetic aperture radar interferometry time series analysis: probing the lithosphere rheological structure, *J. geophys. Res.,* **112**(B3), doi:10.1029/2006JB004344.

Cavalié, O., Lasserre, C., Doin, M.-P., Peltzer, G., Sun, J., Xu, X. & Shen, Z.-K., 2008. Measurement of interseismic strain across the Haiyuan fault (Gansu, China), by InSAR, *Earth planet. Sci. Lett.,* **275,** 246–257.

Champagnac, J.-D., Yuan, D.-Y., Ge, W.-P., Molnar, P. & Zheng, W.-J., 2010. Slip rate at the north-eastern front of the Qilian Shan, China, *Terra Nova,* **22**(3), 180–187.

Chiles, J.-P. & Delfiner, P., 2009. *Geostatistics: Modeling Spatial Uncertainty,* Vol. 497, John Wiley & Sons.

Deng, Q. *et al.*, 1986. Variations in the geometry and amount of slip on the Haiyuan (Nanxihaushan) fault zone, China and the surface rupture of the 1920 Haiyuan earthquake, in *Earthquake Source Mechanics,* pp. 169–182, eds Das, S., Boatwright, J. & Scholz, C.H., American Geophysical Union.

DeVries, P.M. & Meade, B.J., 2013. Earthquake cycle deformation in the Tibetan plateau with a weak mid-crustal layer, *J. geophys. Res.,* **118**(6), 3101–3111.

Doin, M.-P., Lasserre, C., Peltzer, G., Cavalié, O. & Doubre, C., 2009. Corrections of stratified tropospheric delays in SAR interferometry: validation with global atmospheric models, *J. appl. Geophys.,* **69,** 35–50.

Doin, M.-P. *et al.*, 2011. Presentation of the small baseline NSBAS Processing chain on a case example: the Etna deformation monitoring from 2003 to 2010 using Envisat data, in *Proc. ESA Fringe,* pp. 3434–3437, ESA Communications.

Doin, M.-P., Twardzik, C., Ducret, G., Lasserre, C., Guillaso, S. & Jianbao, S., 2015. InSAR measurement of the deformation around Siling Co Lake: inferences on the lower crust viscosity in central Tibet, *J. Geophys. Res.,* **120**(7), 5290–5310.

Ducret, G., Doin, M.-P., Grandin, R., Lasserre, C. & Guillaso, S., 2014. DEM corrections before Unwrapping in a Small Baseline Strategy for InSAR Time Series Analysis, *IEEE Trans. Geosci. Remote Sens.,* **11,** 696–700.

Gaudemer, Y., Tapponier, P., Meyer, B., Peltzer, G., Shunmin, G., Zhitai, C., Huagung, D. & Cifuentes, I., 1995. Partionning of crustal slip between linked, active faults in the eastern Qilian Shan, and evidence for a major seimic gap, the "Tianzhu gap", on the western Haiyuan Fault, Gansu (China), *Geophys. J. Int.,* **120,** 599–645.

Grandin, R., Doin, M.-P., Bollinger, L., Pinel-Puysségur, B., Ducret, G., Jolivet, R. & Sapkota, S.N., 2012. Long-term growth of the Himalaya inferred from interseismic InSAR measurement, *Geology,* **40**(12), 1059–1062.

Hetland, E. & Simons, M., 2010. Post-seismic and interseismic fault creep II: transient creep and interseismic stress shadows on megathrusts, *Geophys. J Int.,* **181**(1), 99–112.

Hooper, A., Segall, P. & Zebker, H., 2007. Persistent scatterer interferometric synthetic aperture radar for crustal deformation analysis, with application to Volcán Alcedo, Galápagos, *J. geophys. Res.,* **112**(B7), doi:10.1029/2006JB004763.

Hu, X. *et al.*, 2015. Rates and kinematics of active shortening along the eastern Qilian Shan, China, inferred from deformed fluvial terraces, *Tectonics,* **34,** 2478–2493.

Jaeger, J.-J., Courtillot, V. & Tapponnier, P., 1989. Paleontological view of the ages of the Deccan Traps, the Cretaceous/Tertiary boundary, and the India-Asia collision, *Geology,* **17**(4), 316–319.

Jolivet, R., Grandin, R., Lasserre, C., Doin, M.-P. & Peltzer, G., 2011. Systematic InSAR tropospheric phase delay corrections from global meteorological reanalysis data, *Geophys. Res. Lett.,* **38,** doi:10.1029/2011GL048757.

Jolivet, R. *et al.*, 2012. Shallow creep on the Haiyuan Fault (Gansu, China) observed by SAR Interferometry, *J. geophys. Res.,* **117,** doi:10.1029/2011JB008732.

Jolivet, R., Lasserre, C., Doin, M.-P., Peltzer, G., Avouac, J.-P., Jianbao, S. & Dailu, R., 2013. Spatio-temporal evolution of aseismic slip along the Haiyuan fault, China: implications for fault frictional properties, *Earth planet. Sci. Lett.,* **377–378,** 23–33.

Jolivet, R., Agram, P.S., Lin, N.Y., Simons, M., Doin, M.-P., Peltzer, G. & Li, Z., 2014. Improving InSAR geodesy using global atmospheric models, *J. geophys. Res.,* **119**(3), 2324–2341.

Jolivet, R., Candela, T., Lasserre, C., Renard, F., Klinger, Y. & Doin, M.-P., 2015a. The burst-like behavior of aseismic slip on a rough fault: the creeping section of the Haiyuan Fault, China, *Bull. seism. Soc. Am.,* **105**(1), 480–488.

Jolivet, R., Simons, M., Agram, P., Duputel, Z. & Shen, Z.-K., 2015b. Aseismic slip and seismogenic coupling along the central san andreas fault, *Geophys. Res. Lett.,* **42**(2), 297–306.

Lasserre, C., 2000. Fonctionnement sismique, cinématique et histoire géologique de la faille de Haiyuan (Chine), *PhD thesis,* Université Paris-Diderot-Paris VII.

Lasserre, C., Bukchin, B., Bernard, P., Tapponnier, P., Gaudemer, Y., Mostinsky, A. & Dailu, R., 2001. Source parameters and tectonic origin of the 1996 june 1 Tianzhu ($M_w = 5.2$) and 1995 July Yongden ($M_w = 5.6$) earthquakes near the Haiyuan fault (Gansu, China), *Geophys. J. Int.,* **144,** 206–220.

Lasserre, C. *et al.*, 2002. Fast late Pleistocene slip rate on the Leng Long Ling segment of the Haiyuan fault, Qinghai, China, *J. geophys. Res.,* **107,** ETG 4-1–ETG 4-15.

Lasserre, C., Peltzer, G., Crampé, F., Klinger, Y., Van der Woerd, J. & Tapponnier, P., 2005. Coseismic deformation of the 2001 $M_w = 7.8$ Kokoxili earthquake in Tibet, measured by synthetic aperture radar interferometry, *J. geophys. Res.,* **110**(B12), doi:10.1029/2004JB003500.

Liang, S., Gan, W., Shen, C., Xiao, G., Liu, J., Chen, W., Ding, X. & Zhou, D., 2013. Three-dimensional velocity field of present-day crustal motion of the Tibetan Plateau derived from GPS measurements, *J. geophys. Res.,* **118**(10), 5722–5732.

Liu-Zeng, J., Klinger, Y., Xu, X., Lasserre, C., Chen, G., Chen, W., Tapponnier, P. & Zhang, B., 2007. Millennial Reccurrence of Large Earthquakes on the Haiyuan Fault near Songshan, Gansu Province, China, *Bull. seism. Soc. Am.,* **97**(1B), 14–34.

Lohman, R.B. & Simons, M., 2005. Some thoughts on the use of InSAR data to constrain models of surface deformation: noise structure and data downsampling, *Geochem. Geophys. Geosyst.,* **6**(1), doi:10.1029/2004GC000841.

López-Quiroz, P., Doin, M.-P., Tupin, F., Briole, P. & Nicolas, J.-M., 2009. Time series analysis of Mexico City subsidence constrained by radar interferometry, *J. Appl. Geophys.,* **69**(1), 1–15.

Loveless, J. & Meade, B.J., 2011. Partitioning of localized and diffuse deformation in the Tibetan Plateau from joint inversions of geologic and geodetic observations, *Earth planet. Sci. Lett.,* **303**(1), 11–24.

McCaffrey, R., 2002. Crustal block rotations and plate coupling, in *Plate Boundary Zones,* pp. 101–122, eds Stein, S. & Freymueller, J.T., American Geophysical Union.

Meade, B.J., 2007. Present-day kinematics at the India-Asia collision zone, *Geology,* **35**(1), 81, doi:10.1130/G22924A.1.

Meade, B.J., Klinger, Y. & Hetland, E.A., 2013. Inference of Multiple Earthquake-Cycle Relaxation Timescales from Irregular Geodetic Sampling of Interseismic Deformation, *Bull. seism. Soc. Am.,* **103**(5), 2824–2835.

Metropolis, N., Rosenbluth, A.W., Rosenbluth, M.N., Teller, A.H. & Teller, E., 1953. Equation of state calculations by fast computing machines, *J. Chem. Phys.,* **21**(6), 1087–1092.

Meyer, B., Tapponnier, P., Bourjot, L., Metivier, F., Gaudemer, Y., Peltzer, G., Shunmin, G. & Zhitai, C., 1998. Crustal thickening in Gausu-Qinghai, lithospheric mantle subduction, and oblique, strike-slip controlled growth of the Tibet plateau, *Geophy. J. Int.,* **135,** 1–47.

Minson, S., Simons, M. & Beck, J., 2013. Bayesian inversion for finite fault earthquake source models. I: Theory and algorithm, *Geophys. J. Int.,* **194**(3), 1701–1726.

Molnar, P. & Tapponnier, P., 1975. Cenozoic tectonics of Asia: effects of a continental collision, *Science,* **189,** 419–426.

Patil, A., Huard, D. & Fonnesbeck, C.J., 2010. PyMC: Bayesian stochastic modelling in Python, *J. Stat. Softw.,* **35**(4), 1–81.

Pinel-Puyssegur, B., Michel, R. & Avouac, J.-P., 2012. Multi-Link InSAR Time Series: Enhancement of a Wrapped Interferometric Database, *IEEE J. Sel. Top. Appl. Earth Obs. Remote Sens.,* **5**(3), 784–794.

Rosen, P.A., Hensley, S., Peltzer, G. & Simons, M., 2004. Updated repeat orbit interferometry package released, *EOS, Trans. Am. geophys. Un.,* **85**(5), 47–47.

Shen, Z.-K. *et al.*, 2009. Slip maxima at fault junctions and rupturing of barriers during the 2008 wenchuan earthquake, *Nat. Geosci.,* **2**(10), 718–724.

Socquet, A., Vigny, C., Chamot-Rooke, N., Simons, W., Rangin, C. & Ambrosius, B., 2006. India and Sunda plates motion and deformation along their boundary in Myanmar determined by GPS, *J. geophys. Res.,* **111**(B5), doi:10.1029/2005JB003877.

Sudhaus, H. & Sigurjón, J., 2009. Improved source modelling through combined use of InSAR and GPS under consideration of correlated data errors: application to the June 2000 Kleifarvatn earthquake, Iceland, *Geophys. J. Int.,* **176**(2), 389–404.

Suppe, J., 1983. Geometry and kinematics of fault-bend folding, *Am. J. Sci.,* **283**(7), 684–721.

Tapponnier, P. & Molnar, P., 1977. Active Faulting and Tectonics in China, *J. geophys. Res.,* **82**(20), 2905–2927.

Tapponnier, P. *et al.*, 1990. Active thrusting and folding in the Qilian Shan, and decoupling between upper crust and mantle in northeastern Tibet, *Earth planet. Sci. Lett.,* **97**(3), 382–403.

Tapponnier, P., Zhiqin, X., Roger, F., Meyer, B., Arnaud, N., Wittlinger, G. & Jingsui, Y., 2001. Oblique Stepwise Rise and Growth of the Tibet Plateau, *Science,* **294**(5547), 1671–1677.

Thatcher, W., 2007. Microplate model for the present-day deformation of Tibet, *J. geophys. Res.,* **112**(B1), B01401, doi:10.1029/2005JB004244.

Thompson, S.C., Weldon, R.J., Rubin, C.M., Abdrakhmatov, K., Molnar, P. & Berger, G.W., 2002. Late Quaternary slip rates across the central Tien Shan, Kyrgyzstan, central Asia, *J. geophys. Res.,* **107**(B9), ETG 7-1–ETG 7-32.

Thompson, T.B., Plesch, A., Shaw, J.H. & Meade, B.J., 2015. Rapid slip-deficit rates at the eastern margin of the Tibetan Plateau prior to the 2008 Mw 7.9 Wenchuan earthquake, *Geophys. Res. Lett.,* **42**(6), 1677–1684.

Trubienko, O., Fleitout, L., Garaud, J.-D. & Vigny, C., 2013. Interpretation of interseismic deformations and the seismic cycle associated with large subduction earthquakes, *Tectonophysics,* **589,** 126–141.

Wang, Q. *et al.*, 2001. Present-day crustal deformation in China constrained by global positioning system measurements, *Science,* **294**(5542), 574–577.

Ye, Z., Gao, R., Li, Q., Zhang, H., Shen, X., Liu, X. & Gong, C., 2015. Seismic evidence for the North China plate underthrusting beneath northeastern Tibet and its implications for plateau growth, *Earth planet. Sci. Lett.,* **426,** 109–117.

SUPPORTING INFORMATION

Additional Supporting Information may be found in the online version of this paper:

Figure S1. Computed interferograms from 31 images along track 104. Triangles are SAR acquisitions, with sizes and colours according to their spatial extend: black triangles for a full coverage and green triangles for images covering the northern part of the track only.

Figure S2. GPS referencing. (a) Subset of 13 reference stations used to define a reference frame south of the Haiyuan Fault. (b) Residual velocities between the observations and the predictions. Faults map and colours as Fig. 1. Insert at the bottom left shows the location of the figure.

Figure S3. Top: Example of two wrapped interferograms (A:20090901-20100119 and B:20050125-20050927), multi-looked by a factor of 4, before (A1-B1) and after (A2-B2) atmospheric corrections predicted using the ERA-I model. Digital Elevation Model is shown in C. Bottom: comparison of the local ratio phase/elevation as a function of elevation before and after correction. Each blue dot corresponds to a local estimate in a sub-window of $\sim$17 km^2.

Figure S4. (A) Map of the DEM error coefficient (in rad m^{-1}) (left). The error δh is 11 m on average. Average temporal coherence map (right) across the pull-apart basin. (B) Effect of local DEM correction for two interferograms with large perpendicular baseline across the Tianzhu pull-apart basin before (left) and after (right) DEM errors correction.

Figure S5. Quality of the LOS velocity map. (A) Estimation of the local velocity–elevation ratios. Top: LOS velocity map (left) and Digital Elevation Model (DEM, right). Bottom: local velocity–elevation ratios as a function of elevation. Each blue dot corresponds to the average velocity–elevation ratio in a local subwindow of 17 $\times$ 14.5 km. (B) Root-mean-square (RMS) network misclosure map between the interferometric phase and the reconstructed phase from time-series inversion (Doin *et al.* 2011). The LOS velocity map in Fig. 3 has been masked on pixels with RMS superior to 0.4 rad, that may be contaminated by errors and phase noise.

Figure S6. Schematic decomposition of each dislocation forming the inverse model for the western (A) and eastern profiles (B). Strike-slip on the Haiyuan and Gulang dislocations are semi-infinite to model the far-field displacements and reproduce rigid-blocks. In case B, slip on the décollement is the sum of $\dot{U}_{s1}$ and $\dot{U}_{s2}$ to ensure the compatibility of the strike-slip motion between the ramp and the décollement. In contrary, slip on the vertical dislocation, $\dot{U}_c$, is inferior or equal to $\dot{U}_{s1}$, allowing for a slip deficit on the creeping

segment. In both cases, the dip-slip motion, $\dot{U}_d$, is the projection of the shortening component on the ramp.

Figure S7. Distribution of the residual between a preliminary model and the InSAR data for InSAR tracks 104 (A1) and 333 (B1). Empirical covariance and associated best-fit exponential functions for the InSAR residual velocity maps (A2, B2). Associated data covariance matrix built from the exponential functions for points sampled in the studied profiles (A3, B3).

Figure S8. Joint inversion map of the GPS and InSAR data across the western (PP) and the eastern (QQ) profiles covered respectively by the track 104 (A) and 333 (B). GPS network is referred to the southern block. InSAR positive motion is away from the satellite. Red dashed lines are associated to 2-D dislocation lines for each fault segment and extract from Figs 4 and 5. The Jing Qiang He (JQH) segment, the Lao Hu Shan (LHS) segment, the Qilian shan Thrusts (QT) and the Gulang Fault (GF) represent the faults segments used in our model.

Figure S9. Joint PDFs for the western (A) and eastern profiles (B) showing trade-offs between some parameters. For the western profile (A) the strike-slip rate of the Haiyuan Fault, $\dot{U}_{s1}$, indicates a correlation with the locking depth, H_1, (left) and with the InSAR azimuthal ramp (right). For the eastern profile (B), joints PDFs reveal a correlation between the InSAR ramp and the strike-slip rates of the Haiyuan Fault, $\dot{U}_{s1}$, (left) as well as between the InSAR azimutal ramp and the shortening component across the fault system, $\dot{U}_{\text{short}}$ (right).

Table S1. Summary of the prior probability distributions (first column), the posterior 95 per cent confidence intervals (second column), as well as the mean, the variance and the skewness (third, fourth and fifth columns) of the marginal posterior distributions for the western (top) and eastern (bottom) profiles.

Table S2. Correlation coefficient matrix of the western profile parameters.

Table S3. Correlation coefficient matrix of the eastern profile parameters.

(http://gji.oxfordjournals.org/lookup/suppl/doi:10.1093/gji/ggw028/-/DC1).

Please note: Oxford University Press is not responsible for the content or functionality of any supporting materials supplied by the authors. Any queries (other than missing material) should be directed to the corresponding author for the paper.